Eur. Phys. J. C (2025) 85:1204
https://doi.org/10.1140/epjc/s10052-025-14974-5

THE EUROPEAN PHYSICAL JOURNAL C

Regular Article - Theoretical Physics

Spin effects on charged particle motion in magnetized Reissner–Nordström spacetime

Tursinbay Oteev[1,2,a], **Zdeněk Stuchlík**[3,b], **Murat Sharibaev**[2,c], **Javlon Rayimbaev**[4,5,6,7,d], **Inomjon Ibragimov**[8,e], **Yunus Turaev**[9,f], **Murodbek Vapayev**[10,g]

[1] Nukus State Pedagogical Institute, Seyitov St. 104, 230100 Nukus, Uzbekistan
[2] Karakalpak State University, Sh.Abdirov 1, 230112 Nukus, Uzbekistan
[3] Research Centre for Theoretical Physics and Astrophysics, Institute of Physics, Silesian University in Opava, Bezručovo nám. 13, 74601 Opava, Czech Republic
[4] Institute of Fundamental and Applied Research, National Research University TIIAME, Kori Niyoziy 39, 100000 Tashkent, Uzbekistan
[5] University of Tashkent for Applied Sciences, Str. Gavhar 1, 100149 Tashkent, Uzbekistan
[6] National University of Uzbekistan, 100174 Tashkent, Uzbekistan
[7] Tashkent State Technical University, 100095 Tashkent, Uzbekistan
[8] Shota Rustaveli street 156, 100121 Tashkent, Uzbekistan
[9] Mamun University, Bolkhovuz Street 2, 220900 Khiva, Uzbekistan
[10] Urgench State University, Kh. Alimjan Str. 14, 221100 Urgench, Uzbekistan

Received: 16 August 2025 / Accepted: 21 October 2025

Abstract This study investigates the dynamics of spinning charged test particles in the spacetime of a Reissner–Nordström (RN) black hole immersed in an asymptotically uniform magnetic field, using the Mathisson–Papapetrou–Dixon (MPD) equations supplemented with the Tulczyjew spin condition. We derive the equations of motion incorporating spin-curvature coupling, electromagnetic interactions, and magnetic field effects, leading to an effective potential that governs equatorial circular orbits. The analysis focuses on how particle spin s, charge q, black hole charge Q, and magnetic coupling ω modify the effective potential, innermost stable circular orbits (ISCO), critical angular momentum for capture, and center-of-mass energy in particle collisions. The obtained results show that a positive spin flattens the potential and shifts the minima inward, enabling closer orbits, while a negative spin steepens it for repulsion. ISCO radii decrease with aligned spin and magnetic coupling, reducing specific energy and angular momentum. Critical angular momentum increases with magnetic strength and charge, exhibiting non-monotonic spin dependence due to competing Lorentz and spin-curvature forces. For collisions, the center-of-mass energy spikes near the horizon, enhanced by opposite spins and counter-rotating orbits, but suppressed by strong magnetic repulsion. At ISCO, energies peak for weak or negative coupling. These findings reveal that spin-magnetic interactions expand stable orbital regimes and boost collision energies, with implications for high-energy astrophysics near magnetized charged black holes, such as particle acceleration in accretion disks or cosmic ray production. We treat the external magnetic field as a test field on a fixed RN geometry and assume it is sufficiently weak at the ISCO so that backreaction is negligible. Scans labeled by $\omega = qB_0$ are evaluated at fixed small B_0 by varying the particle charge q; for ISCO collisions, the first and the second particle orbit and collide at the same ISCO radius.

1 Introduction

Extreme mass ratios in astrophysical configurations, such as those found near the galactic center, allow for approximate analytic descriptions of particle motion under specific parameter constraints. Increasingly improving observational capabilities, particularly in monitoring stellar orbits around Sagittarius A*, have yielded increasingly precise data on the gravitational environment near the galactic center [1,2]. These

[a] e-mail: oteevtp@gmail.com
[b] e-mail: zdenek.stuchlik@fpf.slu.cz
[c] e-mail: sharibaev.m.b@gmail.com
[d] e-mail: javlon@astrin.uz (corresponding author)
[e] e-mail: i.ibragimov@kiut.uz
[f] e-mail: yunus.turaev.nw@gmail.com
[g] e-mail: murodbek.v@urdu.uz

Published online: 25 October 2025

advancements highlight the relevance of theoretical studies on relativistic particle dynamics near compact astrophysical objects. In this work, we investigate the motion of spinning charged test particles in the background of a Reissner–Nordström black hole immersed in an external, asymptotically uniform magnetic field. In what follows, we work strictly in the test-field regime for the external magnetic field: in geometrized units, backreaction on the RN geometry is negligible provided $(B_0\,\mathcal{L})^2 \ll 1$ with $\mathcal{L} \sim r_{\rm ISCO} = O(M)$. Since particle dynamics depend on the dimensionless coupling $\omega \equiv q B_0$ whereas geometric backreaction depends only on B_0^2, variations of ω in our plots are realized at fixed small B_0 by adjusting the specific charge q, so the scans represent the equivalence class of pairs (q, B_0) with $q B_0 = \omega$.

The motion of spinning test particles in curved spacetime was first considered by Mathisson [3], who laid the foundation for modeling extended bodies in general relativity (GR). This framework was subsequently developed by Papapetrou, Tulczyjew, and others [4–9], leading to the formulation of the Mathisson–Papapetrou–Dixon (MPD) equations [10–12], which govern the dynamics of spinning particles in gravitational fields. The MPD formalism has since been refined in more recent studies [13–15], particularly through the application of spin-supplementary conditions, such as the Tulczyjew condition. Contemporary works have applied these equations to black hole spacetimes, providing new insights into the effects of spin on test particle motion [16]. Further studies have explored spin-induced phenomena in various settings, including charged and rotating black holes and configurations with external fields [17–30] A full Einstein–Maxwell treatment of charged black holes immersed in external magnetic fields exists in the literature; our aim here is complementary, focusing on the probe-field limit on an exact RN background, which is the regime relevant for the parameter scans presented below.

Analytical solutions play a crucial role in gravitational physics. They not only serve as a foundation for developing and validating numerical approaches, but also allow for systematic exploration of parameter spaces relevant to astrophysical observations. Recent studies, such as [30], have highlighted exact analytical solutions for particle geodesics, demonstrating their practical utility. Many of these solutions rely on the mathematical framework of elliptic functions and modular forms–fields pioneered by nineteenth-century mathematicians such as Jacobi [31], Abel [32], Riemann [33,34], and Weierstrass [35]. A comprehensive overview of these classical developments can be found in Ref. [36]. In contemporary research, techniques based on modular and elliptic functions have been widely employed to evaluate elliptic integrals that appear in relativistic orbital dynamics. This approach has been successfully applied to analyze particle trajectories in strong gravitational fields, particularly around black holes [28–30].

This manuscript investigates the dynamics of charged spinning test particles orbiting a Reissner–Nordström black hole background immersed in an asymptotically uniform magnetic field. We present a comprehensive analysis of how spin-curvature coupling and electromagnetic interactions influence both circular motion and high-energy particle collisions. Our study is organized as follows: in Sect. 2, we develop the theoretical framework by extending the Mathisson–Papapetrou–Dixon (MPD) equations to include external magnetic fields. This formulation yields the conserved quantities of motion and enables the derivation of the effective potential, for which we establish precise timelike motion conditions, including the superluminal bound. Section 3 examines spin and magnetic effects on the effective potential, with particular focus on modifications to the innermost stable circular orbits (ISCOs). Section 4 investigates high-energy collisions between charged spinning particles, quantifying how spin-magnetic coupling impacts the center-of-mass energy. We conclude in Sect. 5 by discussing the physical implications of our results for astrophysical scenarios involving magnetized black holes. For clarity in the figures, parameters are displayed in terms of ω; unless stated otherwise, this should be understood as an equivalence class of (q, B_0) pairs with $q B_0 = \omega$ realized at fixed small B_0 in the test-field regime.

Throughout our analysis, we employ geometrized units ($G = c = 1$) and work with dimensionless quantities for clarity and consistency. The combined treatment of spin-curvature and electromagnetic effects provides new insights into relativistic dynamics in strongly magnetized spacetimes.

2 Test spinning charged particle motion

In this section, we derive the equations of motion governing a charged spinning test particle in the background of an RN black hole immersed in an asymptotically uniform magnetic field. The magnetic field is treated as a test field: it does not backreact on the geometry but it does act on the particle through the electromagnetic four-potential.

The exterior geometry of an RN black hole with mass M and electric charge Q is

$$ds^2 = -f(r)\,dt^2 + \frac{dr^2}{f(r)} + r^2\left(d\theta^2 + \sin^2\theta\, d\phi^2\right), \qquad (1)$$

with lapse

$$f(r) = 1 - \frac{2M}{r} + \frac{Q^2}{r^2}. \qquad (2)$$

The electrostatic potential of the RN black hole has a single nonvanishing component,

$$A_t = -\frac{Q}{r}. \tag{3}$$

2.1 Magnetic field solution in Reissner–Nordström spacetime

We now place the RN black hole in an asymptotically uniform magnetic field aligned with the symmetry axis. The field is taken as a test solution of the source-free Maxwell equations on the fixed RN background and adds an azimuthal component to the four-potential that influences charged motion.

Following Wald's [37] construction for axially symmetric backgrounds, we use the ansatz [38–42]

$$A_\phi = \frac{1}{2} B_0\, \psi(r)\, \sin^2\theta, \tag{4}$$

where B_0 is the magnetic field measured at spatial infinity and $\psi(r)$ is determined from the source-free Maxwell equations

$$\frac{1}{\sqrt{-g}}\partial_\alpha\left(\sqrt{-g}\, F^{\alpha\beta}\right) = 0, \quad F_{\alpha\beta} = \partial_\alpha A_\beta - \partial_\beta A_\alpha. \tag{5}$$

Substituting (4) into (5) gives

$$r^2 f(r)\, \psi''(r) + 2\left(M - \frac{Q^2}{r}\right)\psi'(r) - 2\,\psi(r) = 0. \tag{6}$$

Solving (6) in dimensionless variables $r \to r/M$ and $Q \to Q/M$ (so $M = 1$) and selecting the branch that approaches a uniform field at infinity yields

$$\psi(r) = r^2 - Q^2, \tag{7}$$

which reduces to $\psi(r) = r^2$ in the Schwarzschild limit $Q \to 0$, as expected from Wald's solution.

The total electromagnetic four-potential is therefore

$$A_\mu = \left\{-\frac{Q}{r},\, 0,\, 0,\, \frac{B_0}{2}\,(r^2 - Q^2)\sin^2\theta\right\}, \tag{8}$$

so that $A_\phi \sim \frac{B_0}{2} r^2 \sin^2\theta$ as $r \to \infty$ and B_0 indeed coincides with the magnetic field at infinity. Throughout we work in the weak field regime, neglecting the Maxwell stress energy of the external field; in practice, this means $|B_0|M \ll 1$, while $\omega_i = q_i B_0$ in the figures is realized by adjusting q_i at a fixed small B_0, so the coupling ω_i itself need not be small.

2.2 The effective potential for a charged spinning particle's motion

The effects of external magnetic fields on the dynamics of charged test particles are crucial in black hole spacetimes. The motion and radiation of charged particles around magnetized black holes, including the influence of radiation reaction forces, have been extensively studied in [43,44]. Furthermore, the combined impact of spin and magnetic fields on the dynamics of magnetized particles near black holes presents a rich phenomenology and continues to attract considerable attention. In this work, the external magnetic field is treated as a test field on a fixed Reissner–Nordström background; in geometrized units, backreaction is negligible provided the field is sufficiently weak in the region of interest, for example, at the ISCO. Accordingly, parameter scans labeled by $\omega \equiv q B_0$ are interpreted at fixed small B_0, with ω realized by varying the test particle's specific charge q.

In this work, we investigate the dynamics of a spinning charged test particle orbiting a magnetized RN black hole. In general relativity, the equations of motion for spinning particles deviate from the standard geodesic equation because of the spin-curvature coupling, an interaction between the particle's spin tensor and the background Riemann curvature tensor. This coupling plays a significant role in strong gravitational fields such as those near black holes [3–5]. Throughout we confine attention to timelike worldlines ($v^\mu v_\mu < 0$) and later impose the standard causality or superluminal bound when analyzing circular motion and the effective potential.

The equations of motion for a charged spinning test particle in a curved space-time background with an external electromagnetic field are described by the modified Mathisson–Papapetrou–Dixon (MPD) equations, which incorporate the Lorentz force due to the electromagnetic field. Although a spinning charged particle has an intrinsic magnetic moment, we follow previous work and neglect this contribution, assuming that the dominant electromagnetic interaction arises from the Lorentz force exerted by the external field on the particle's charge [45]. This approximation is valid when the dipole coupling to field gradients is subleading relative to the Lorentz term in the parameter ranges considered here. The resulting equations of motion are given by

$$\frac{Dp^\alpha}{d\lambda} = -\frac{1}{2} R^\alpha{}_{\beta\rho\sigma} v^\beta S^{\rho\sigma} - mq F^\alpha{}_\beta v^\beta, \tag{9}$$

$$\frac{DS^{\alpha\beta}}{d\lambda} = p^\alpha v^\beta - v^\alpha p^\beta, \tag{10}$$

where $D/d\lambda$ denotes the covariant derivative along the worldline of the particle, $v^\alpha = dx^\alpha/d\lambda$ is the four-velocity of the particle, p^α is the canonical four-momentum, q is the electric charge of the particle, and m is the dynamic mass defined by the normalization condition $m^2 = -p_\alpha p^\alpha$. The electromagnetic field tensor $F_{\mu\nu}$ includes contributions from both the intrinsic charge of the black hole and the external magnetic field, while $R^\alpha{}_{\beta\rho\sigma}$ is the Riemann curvature tensor. The spin tensor $S^{\alpha\beta}$ is antisymmetric, satisfying $S^{\alpha\beta} = -S^{\beta\alpha}$. In particular, $F_{\mu\nu}$ combines the RN electric

field sourced by Q with the asymptotically uniform external magnetic field of amplitude B_0, the latter being kept small so that the background geometry remains RN.

Equation (9) explicitly illustrates the gravitational spin-curvature coupling, which modifies the motion of the particle relative to the geodesic trajectories. To clarify this deviation, recall the standard geodesic equation in general relativity:

$$v^\beta \partial_\beta v^\alpha + \Gamma^\alpha_{\sigma\beta} v^\sigma v^\beta = 0. \tag{11}$$

Rewriting Eq. (11) in terms of the covariant derivative of the four-momentum, one obtains:

$$\frac{Dp^\alpha}{d\lambda} = 0, \tag{12}$$

which corresponds to the geodesic motion of a spinless neutral particle.

By comparing Eqs. (9) and (12), one sees the additional terms in Eq. (9), namely the spin-curvature coupling term involving the Riemann tensor and the Lorentz force term proportional to $q F^\alpha_\beta v^\beta$. These terms illustrate how the presence of spin and electric charge alters the trajectory of the particle, causing it to deviate from the geodesic path followed by a neutral, non-spinning particle. Below, we specialize to equatorial motion when constructing the effective potential and identifying circular orbits and their stability.

A crucial aspect of the MPD equations concerns the definition of the center of mass for the spinning particle. To obtain a determinate evolution of the system described by Eqs. (9) and (9), one must impose a supplementary condition that fixes the representative worldline of the particle. This is achieved by adopting the Tulczyjew spin supplementary condition (SSC) [6,46]:

$$S^{\alpha\beta} p_\alpha = 0. \tag{13}$$

The condition in Eq. (13) ensures that the spin tensor is orthogonal to the four-momentum and effectively selects the center-of-mass frame of the particle. From this constraint, one obtains two independent conserved quantities: the canonical four-momentum and the magnitude of the spin, expressed as

$$p^\alpha p_\alpha = -m^2, \tag{14}$$
$$S^{\alpha\beta} S_{\alpha\beta} = 2S^2 = 2m^2 s^2, \tag{15}$$

where m is the dynamical mass of the particle and s is the specific spin parameter per unit mass. These ingredients allow us to recast the radial dynamics into an effective potential for equatorial circular motion, subject to the timelike and causality constraints noted above.

2.3 Estimating spin parameter for astrophysical objects

One may estimate the spin parameter for rotating neutron stars, with rotational angular momentum $S = I\Omega$, where $\Omega = 2\pi/P$ and P is the rotational period, as

$$s_{\rm NS} = \frac{I\Omega}{m_{\rm NS} M_{BH}}, \tag{16}$$

where I is the moment of inertia of the star. In Newtonian gravity, the moment of inertia of a massive spherical object is $I = (2/5) m_{NS} R^2$. As we consider neutron stars composed of uniform dense stiff matter with $\rho = $ const, their moment of inertia does not change much due to rotation and surface gravity [47].

For a millisecond neutron star orbiting an intermediate-mass black hole, the spin parameter is

$$s \simeq 6 \times 10^{-3} \left(\frac{R^2}{10^6\,{\rm cm}}\right)^2 \frac{10^4 M_\odot}{M} \frac{1\,{\rm ms}}{P}\,. \tag{17}$$

For a system consisting of a stellar-mass black hole and an intermediate-mass black hole,

$$s \simeq 10^{-3} \frac{a}{M} \frac{M}{10 M_\odot} \frac{10^4 M_\odot}{M_{IMBH}}\,. \tag{18}$$

2.4 Conserved quantities

However, it is important to note that, unlike the canonical momentum, the four-velocity v^α of the spinning particle generally does not satisfy the normalization condition $v_\alpha v^\alpha = -1$, since p^α and v^α are not, in general, parallel. Therefore, to ensure that the motion of the particle remains physically admissible, an additional constraint must be imposed to avoid superluminal behavior, commonly referred to as the *superluminal bound*.

In practice, we enforce this together with the Tulczyjew admissibility condition derived below; taken jointly, these constraints delimit the physical parameter domain for circular motion.

In addition to the conserved quantities derived from the Tulczyjew spin supplementary condition, a charged spinning particle in a stationary and axisymmetric spacetime also possesses conserved quantities associated with the spacetime's Killing symmetries. These arise from the Killing vector of time translation $\xi^\alpha = (\partial_t)^\alpha$ and the axial Killing vector $\psi^\alpha = (\partial_\varphi)^\alpha$. For spinning charged particles, these conserved quantities generalize to the form [48]:

$$C_k = p^\alpha k_\alpha - \frac{1}{2} S^{\alpha\beta} \nabla_\beta k_\alpha + mq k^\alpha A_\alpha, \tag{19}$$

where A_α is the electromagnetic four-potential and k^α is any Killing vector field of the background geometry. We identify the specific energy and total angular momentum as $\mathcal{E} \equiv -C_\xi/m$ and $\mathcal{J} \equiv C_\psi/m$, respectively.

By evaluating Eq. (19) for the time translation and axial Killing vectors, two conserved quantities associated with the test particle's motion are obtained: the specific energy $\mathcal{E}$ and the specific total angular momentum $\mathcal{J}$. Restricting the motion to the equatorial plane ($\theta = \pi/2$), these quantities reduce to

$$-\mathcal{E} = u_t - \frac{1}{2m} g_{tt,r} S^{tr} + q A_t, \tag{20}$$

$$\mathcal{J} = u_\varphi + \frac{1}{2m} g_{\varphi\varphi,r} S^{r\varphi} + q A_\varphi. \tag{21}$$

Here $A_t = -Q/r$ and $A_\varphi = \frac{1}{2} B_0 \psi(r) \sin^2\theta$ with $\psi(r) = r^2 - Q^2$; on the equator $\sin^2\theta = 1$.

Here we define specific (mass-rescaled) quantities as $\mathcal{E} = E/m$, $\mathcal{J} = J/m$, $s = S/m$, and $u_\mu = p_\mu/m$. The coupling to the magnetic field is encoded in the dimensionless parameter $\omega = q B_0$. In particular, in the Schwarzschild limit ($Q = 0$), one recovers the simpler form where $A_t = 0$ and $A_\varphi = \frac{1}{2} B_0 r^2 \sin^2\theta$.

Equation (20) incorporates the electrostatic interaction via A_t, while Eq. (21) reflects the coupling to the external magnetic field through A_φ. These conserved quantities play a central role in deriving the effective potential governing the radial dynamics of the charged spinning particle in the magnetized Reissner–Nordström spacetime.

From Eq. (13), one can derive the following algebraic relations among the components of the spin tensor:

$$S^{t\varphi} = -\frac{p_r}{p_\varphi} S^{tr}, \quad S^{r\varphi} = \frac{p_t}{p_\varphi} S^{tr}. \tag{22}$$

Using Eqs. (14), (15), and (22), we obtain the explicit expressions for the relevant spin components:

$$S^{tr} = \frac{s}{\sqrt{-g_{tt} g_{rr} g_{\varphi\varphi}}} p_\varphi, \quad S^{r\varphi} = \frac{s}{\sqrt{-g_{tt} g_{rr} g_{\varphi\varphi}}} p_t. \tag{23}$$

Restricting the analysis to the equatorial plane ($\theta = \pi/2$), we set the black hole mass to $M = 1$ for simplicity. Then, the metric components of the Reissner–Nordström spacetime take the form:

$$g_{tt} = -f(r), \quad g_{rr} = \frac{1}{f(r)}, \quad g_{\varphi\varphi} = r^2.$$

Substituting into Eq. (23), the spin components simplify to:

$$S^{tr} = \frac{s}{r} p_\varphi, \quad S^{r\varphi} = \frac{s}{r} p_t. \tag{24}$$

The conserved quantities for energy and angular momentum, derived from the Killing symmetries and electromagnetic interaction, are given by:

$$-\mathcal{E} = u_t - \frac{f'(r)}{2r} s u_\varphi - \frac{qQ}{r}, \tag{25}$$

$$\mathcal{J} = u_\varphi - s u_t + \frac{1}{2}\omega(r^2 - Q^2), \tag{26}$$

where $\omega = q B_0$ is the magnetic interaction parameter and $\psi(r) = r^2 - Q^2$ is the structure function appearing in A_φ. Equations (25)–(26) reproduce the familiar Schwarzschild–Wald limit for $Q \to 0$.

Solving Eqs. (25) and (26) for u_t and u_φ, we obtain

$$\mathcal{A}(r) \equiv -\mathcal{E} + \frac{qQ}{r}, \quad \mathcal{B}(r) \equiv \mathcal{J} - \frac{\omega}{2}(r^2 - Q^2),$$

$$u_t = \frac{r^4 \mathcal{A}(r) + s\,(r - Q^2)\,\mathcal{B}(r)}{r^4 - s^2(r - Q^2)}, \tag{27}$$

$$u_\varphi = \frac{r^4 \mathcal{B}(r) + s\, r^4 \mathcal{A}(r)}{r^4 - s^2(r - Q^2)}. \tag{28}$$

The common denominator $r^4 - s^2(r - Q^2)$ is positive in the admissible domain of the Tulczyjew SSC; its vanishing would signal loss of timelike motion and therefore marks the boundary of the physical region.

Now, we rewrite Eq. (14) by dividing both sides by m^2, giving the normalized condition $u^\alpha u_\alpha = -1$. From this, we derive the expression for the radial motion of a spinning charged particle in the magnetized Reissner–Nordström black hole background as:

$$(u^r)^2 = \frac{\rho}{\sigma}\left(\mathcal{E}^2 + \delta\mathcal{E} + \gamma\right), \tag{29}$$

where ρ and σ are positive outside the horizon in the admissible domain, and δ, γ encode spin-curvature and electromagnetic couplings:

$$\rho = r^8\Big(r^4 - s^2\big(Q^2 + r(r-2)\big)\Big), \tag{30}$$

$$\sigma = \big(r^4 - s^2(r - Q^2)\big)^2 \big(Q^2 + r^2 - 2r\big)^2, \tag{31}$$

$$\begin{aligned}\delta = {} & \frac{4s\big(Q^2 + r(r-2)\big)}{r^4 + Q^2 s^2 - r s^2}\Big(\omega r^2 (Q^2 - r^2)\big(Q^2 + r(r-2)\big) \\ & - 2Qqr^3 + 2\mathcal{J}s(Q^2 - r) \\ & + 2\big(Q^2 + r(r-2)\big)\big(Qqs + \mathcal{J}r\big)\Big),\end{aligned} \tag{32}$$

$$\begin{aligned}\gamma = {} & \frac{1}{4r^2\sigma}\Big[\omega^2 r^2 s^2 (Q^2 - r)^2 (Q^2 + r)^2 - \omega^2 r^6 (Q^2 - r^2)^2 \\ & \times \big(Q^2 + r(r-2)\big) - 4\omega r^5 (Q^2 - r^2)\big(Q^2 + r(r-2)\big) \\ & \times \big(qQs + \mathcal{J}r\big) + 4\omega r^2 s (Q^2 - r)^3 (Q^2 + r)^2\end{aligned}$$

$$\times \left(-Qqr^3 + \mathcal{J}s(Q^2 - r)\right) - 4r^4\left(Q^2 + r(r-2)\right)$$
$$\times \left(Q^2q^2s^2 + 2Qq\mathcal{J}rs + \mathcal{J}^2r^2\right)$$
$$+ 4r^2\Big(Q^2q^2r^6 - 2Qq\mathcal{J}r^3s(Q^2 - r) + \mathcal{J}^2s^2(Q^2 - r)^2\Big)$$
$$- 4\left(Q^2 + r(r-2)\right)\left(Q^2s^2 + r^4 - rs^2\right)^2\Big]. \tag{33}$$

In the limit $Q \to 0$ and $\omega \to 0$, these expressions reduce to the known Schwarzschild spinning-particle formulas.

We rewrite Eq. (29) in a factorized form:

$$(u^r)^2 = \frac{\rho}{\sigma}(\mathcal{E} - V_+)(\mathcal{E} - V_-), \tag{34}$$

which enables the definition of the effective potential for circular motion of spinning magnetized particles, characterized by the condition $u^r = 0$, as follows [48]:

$$V_\pm = \frac{-\delta \pm \sqrt{\delta^2 - 4\gamma}}{2}. \tag{35}$$

We focus on positive-energy orbits and take $V_{\text{eff}} = V_+$; physical motion requires $(u^r)^2 \geq 0$ together with the admissibility and causality constraints noted above.

Having established the effective potential, we are now in a position to analyze the influence of spin and magnetic interactions, as well as their combined effects, on the radial dynamics of spinning charged particles. Given the complexity of the expression, this analysis will be carried out graphically in the following sections.

2.5 Superluminal bound

In this subsection, we investigate the superluminal bound. This critical condition determines the range of the spin parameter s for which the trajectory of a spinning test particle remains timelike and physically viable. This ensures that the particle's motion respects causality and remains subluminal throughout its evolution. We begin by deriving general expressions for the superluminal constraint in static and spherically symmetric spacetimes, incorporating spin-curvature coupling as governed by the MPD equations with the Tulczyjew spin supplementary condition. These expressions provide a framework for assessing whether specific values of the spin and other parameters yield a physically consistent, timelike worldline.

Although the four-momentum satisfies the standard normalization $p_\alpha p^\alpha = -m^2$, the same is not necessarily true for the four-velocity v^α due to spin-induced deviations. In general, $v^\alpha \neq p^\alpha/m$, and the norm $v_\alpha v^\alpha$ may differ from -1. For certain combinations of spin s, radial position, and charge-to-mass ratio, the components of v^α can diverge, which violates the timelike condition. Such behavior signals the breakdown of the test particle approximation: the trajectory transitions to a spacelike path, corresponding to motion faster than light, an outcome incompatible with general relativity. To avoid this scenario, an additional constraint must be imposed, requiring that the four-velocity remain timelike: $v_\alpha v^\alpha < 0$.

This inequality defines the superluminal bound and restricts the admissible range of the spin parameter s to ensure causal propagation. Here, we analyze this bound in the context of a RN black hole immersed in an external, asymptotically uniform magnetic field. This setup extends the magnetized Schwarzschild case by accounting for the black hole's electric charge, which alters the spin-curvature and spin-electromagnetic coupling. We examine how this charge modifies the superluminal limit and reshapes the parameter space physically allowed [49].

$$\frac{v_\alpha v^\alpha}{(v^t)^2} = g_{tt} + g_{rr}\left(\frac{dr}{dt}\right)^2 + g_{\varphi\varphi}\left(\frac{d\varphi}{dt}\right)^2 < 0.$$

For circular equatorial motion with $dr/dt = 0$ and $\theta = \pi/2$, this becomes $g_{tt} + g_{\varphi\varphi}\,\Omega^2 < 0$ with $\Omega \equiv d\varphi/dt$.

To incorporate the superluminal bound into our analysis, we require explicit expressions for the radial and angular coordinate velocities, dr/dt and $d\varphi/dt$. To this end, we follow the approach introduced by Hojman and Asenjo [45]. As in our previous works [50,51], we restrict the motion of the particle to the equatorial plane ($\theta = \pi/2$), where the non-vanishing components of the spin tensor $S^{\alpha\beta}$ are S^{tr}, $S^{t\varphi}$ and $S^{r\varphi}$. The coordinate velocities $(dr/dt, d\varphi/dt)$ are obtained by expressing v^μ in terms of p^μ and $S^{\mu\nu}$ under the Tulczyjew SSC and then dividing by v^t; the explicit formulas coincide with those derived in [50,52] and are not repeated here.

Using these expressions, we evaluated the superluminal condition $v_\alpha v^\alpha < 0$ as a function of the spin parameter s and the coupling parameter ω, which encodes the interaction between the particle's charge and the external magnetic field. This analysis enables us to identify the physically admissible range of s for which the trajectory remains timelike. In addition, we enforce the Tulczyjew admissibility condition $r^4 - s^2(r - Q^2) > 0$, which guarantees a positive normalization factor in the relation between v^μ and p^μ and prevents the loss of timelike character.

To visualize the causality constraint, Fig. 1 shows the (ω, s) plane at fixed background and orbital parameters stated in the caption. Here $\omega = qB_0$ quantifies the magnetic coupling and s is the signed spin parameter. The shaded region marks where $v_\alpha v^\alpha < 0$ and the SSC-admissibility condition $r^4 - s^2(r - Q^2) > 0$ are simultaneously satisfied, that is, timelike, physically allowed trajectories. The bounding curve identifies critical pairs (ω, s) beyond which the motion becomes spacelike with $v_\alpha v^\alpha > 0$, violating causality. Its smooth curvature reflects the nonlinear interplay of spin-curvature and magnetic interactions: as $|s|$ increases,

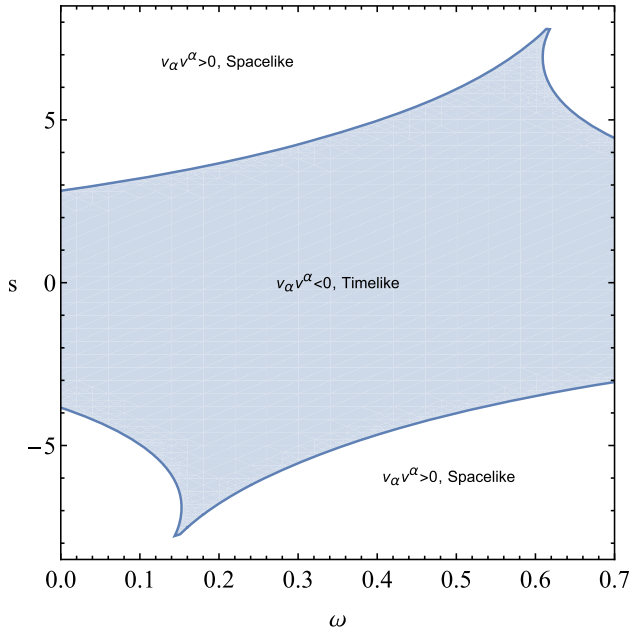

Fig. 1 Causality-preserving region in the (ω, s)-plane for a charged spinning test particle in the background of a magnetized RN black hole. The shaded area corresponds to timelike motion satisfying $v_\alpha v^\alpha < 0$, while the unshaded region corresponds to unphysical, spacelike trajectories

the allowed window in ω narrows and the boundary steepens, while for $\omega \to 0$ it approaches the pure-spin limit. We use the clean field normalization $A_\phi = \frac{B_0}{2}(r^2 - Q^2)\sin^2\theta$ and keep B_0 in the test-field regime; the qualitative trends are robust under moderate changes of $(Q, q, \mathcal{J})$ and of the evaluation radius.

This figure highlights the complex interplay between spin, electromagnetic coupling, and background geometry in the magnetized RN spacetime. Unlike in the Schwarzschild case, the presence of the black hole's electric charge further modifies the spin-curvature and spin-electromagnetic interactions, leading to a richer and more constrained structure of the physically viable parameter space.

3 Dynamics of charged spinning test particles around a magnetized RN black hole

3.1 Effective potential

We analyze the motion of a charged spinning test particle in the spacetime of an RN black hole subjected to an asymptotically uniform magnetic field. This configuration combines gravitational attraction, electromagnetic repulsion or attraction depending on charge signs, and spin-curvature coupling, making the dynamics highly sensitive to both the intrinsic properties of the particle and the black hole parameters. In what follows, we display the effective potential $V_{\rm eff}$ to diagnose circular orbits and their stability as the key parameters are varied one at a time, holding the others fixed.

Figure 2 shows the radial dependence of the effective potential $V_{\rm eff}$ under variations of four key parameters: spin magnitude s, electric charge q, magnetic coupling ω, and black hole charge Q. Each panel isolates the effect of one parameter while holding the others fixed, illustrating how each contributes to the shape of the potential well and the location of circular-orbit minima.

In the upper left panel, the spin parameter s is varied while keeping $\mathcal{J} = 4$, $q = 1$, $Q = 0.5$, and $\omega = 0.01$ fixed. For negative s, the potential becomes shallower and the minimum shifts to larger radii, indicating that spin-curvature coupling pushes the orbit outward. As s increases to positive values (aligned spin), the potential deepens and its minimum moves inward, allowing closer circular orbits.

In the upper right panel, we vary the particle charge q from -0.5 to 0.5 at fixed $s = 0.3$, $Q = 0.5$, and fixed external B_0, so $\omega = qB_0$ varies accordingly. Like charge with $qQ > 0$ raises the potential and shifts the minimum outward due to electrostatic repulsion, whereas opposite charge with $qQ < 0$ deepens the well and pulls the minimum inward.

The bottom left panel examines the dependence on the black hole charge Q for $s = 0.5$, $q = 1$, and $\omega = 0.01$. As Q increases, the background electric field strengthens; for like-charged motion this broadens and shallows the well and moves the minimum outward, reducing the viability of tighter orbits.

The bottom right panel explores the magnetic coupling ω with $s = 0.3$, $q = 1$, and $Q = 0.5$ fixed. Increasing ω strengthens magnetic confinement, deepens the potential, and shifts the minimum inward, whereas decreasing ω weakens binding and moves the minimum outward.

3.2 Innermost stable circular orbits

Although the conditions $\mathcal{E} = V_{\rm eff}$ and $dV_{\rm eff}/dr = 0$ ensure that a particle resides on a circular orbit, they do not by themselves guarantee orbital stability. For a circular orbit to be dynamically stable under small radial perturbations, the effective potential must exhibit a local minimum, which requires the second derivative to be positive: $d^2V_{\rm eff}/dr^2 > 0$. The boundary case where $d^2V_{\rm eff}/dr^2 = 0$ marks the onset of instability and defines the *innermost stable circular orbit* (ISCO), the smallest radius at which a test particle can maintain a stable circular trajectory.

To determine the ISCO parameters, we simultaneously impose the three conditions:

$$V_{\rm eff} = \mathcal{E}, \quad \frac{dV_{\rm eff}}{dr} = 0, \quad \frac{d^2V_{\rm eff}}{dr^2} = 0. \tag{36}$$

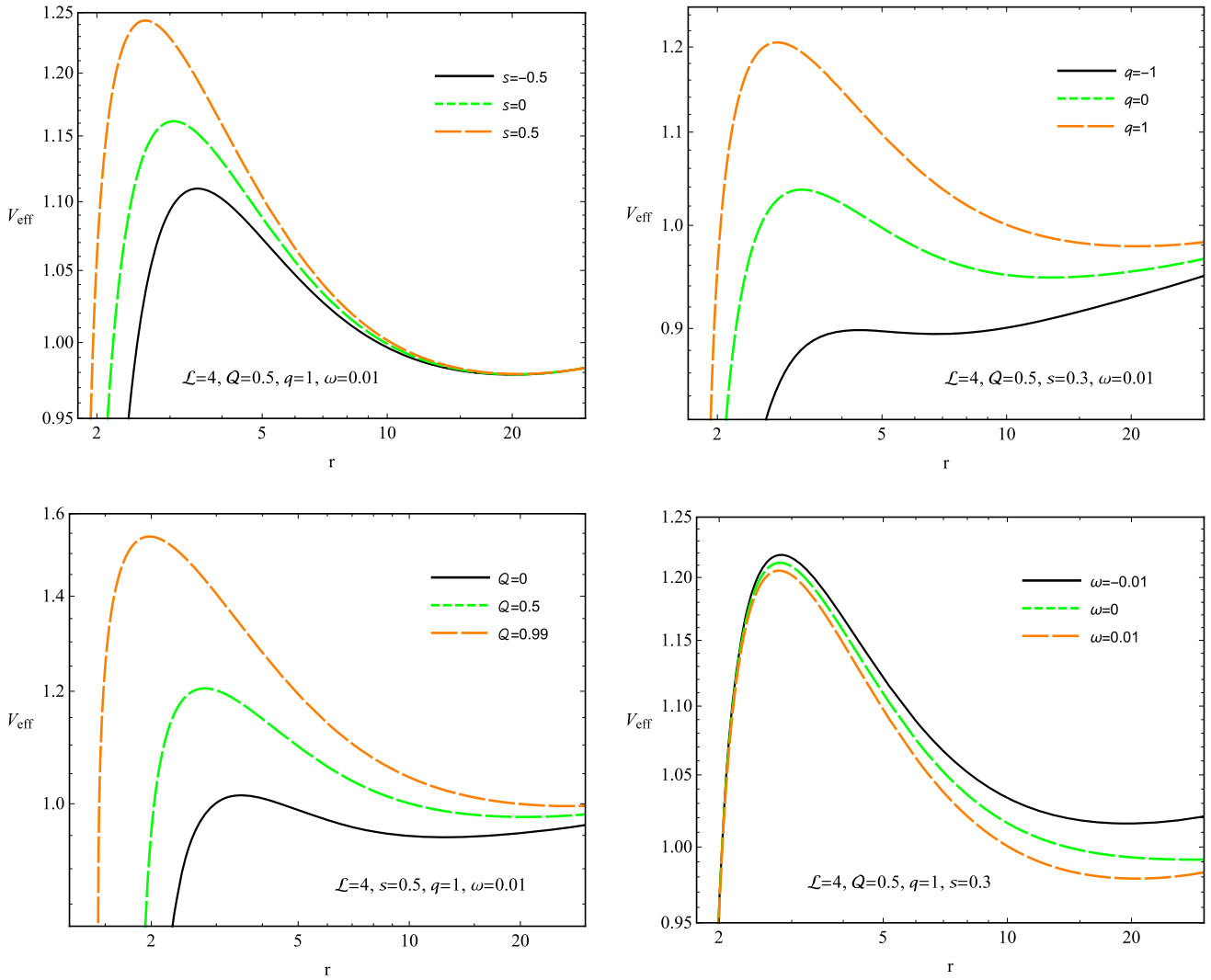

Fig. 2 Radial profiles of the effective potential V_{eff} for a charged, spinning test particle in magnetized Reissner–Nordström spacetime. Upper left: variation of spin s. Upper right: variation of particle charge q. Bottom left: variation of black-hole charge Q. Bottom right: variation of magnetic coupling ω. Each panel varies only the stated parameter; the others are held fixed. When ω is varied, the scan specifies whether the change is implemented via q or B_0; the physics enters through $\omega = qB_0$. Local minima of $V_{\text{eff}}(r)$ mark circular orbits; the loss of the minimum signals the disappearance of the ISCO

This yields the ISCO radius r_{ISCO}, along with the corresponding specific energy $\mathcal{E}_{\text{ISCO}}$ and specific angular momentum $\mathcal{L}_{\text{ISCO}}$. Due to the highly nonlinear nature of these equations, especially in the presence of spin-curvature and electromagnetic interactions, we solve the system numerically and visualize the parameter dependencies.

Figure 3 illustrates how s and $\omega \equiv qB_0$ influence the ISCO through Papapetrou spin-curvature and Lorentz or A_ϕ effects. In the top row, $\mathcal{E}_{\text{ISCO}}$, $\mathcal{L}_{\text{ISCO}}$, and r_{ISCO} all decrease as s increases for aligned spin, with the trend strengthening at larger $|\omega|$. Aligned spin lowers the effective centrifugal barrier and deepens the well, permitting orbits closer to the black hole. Near critical s the curves steepen, signaling proximity to the causality or admissibility boundary.

In the bottom row, the same quantities are plotted against ω for several fixed spins. As ω increases, $\mathcal{E}_{\text{ISCO}}$ and $\mathcal{L}_{\text{ISCO}}$ decrease because the canonical A_ϕ term offsets mechanical angular momentum and the Lorentz force aids confinement. The ISCO radius shows a mild nonmonotonicity at low or zero spin, with a slight initial increase before decreasing, due to competition between the Lorentz push and the A_ϕ offset. For sufficiently positive s, r_{ISCO} decreases monotonically with ω.

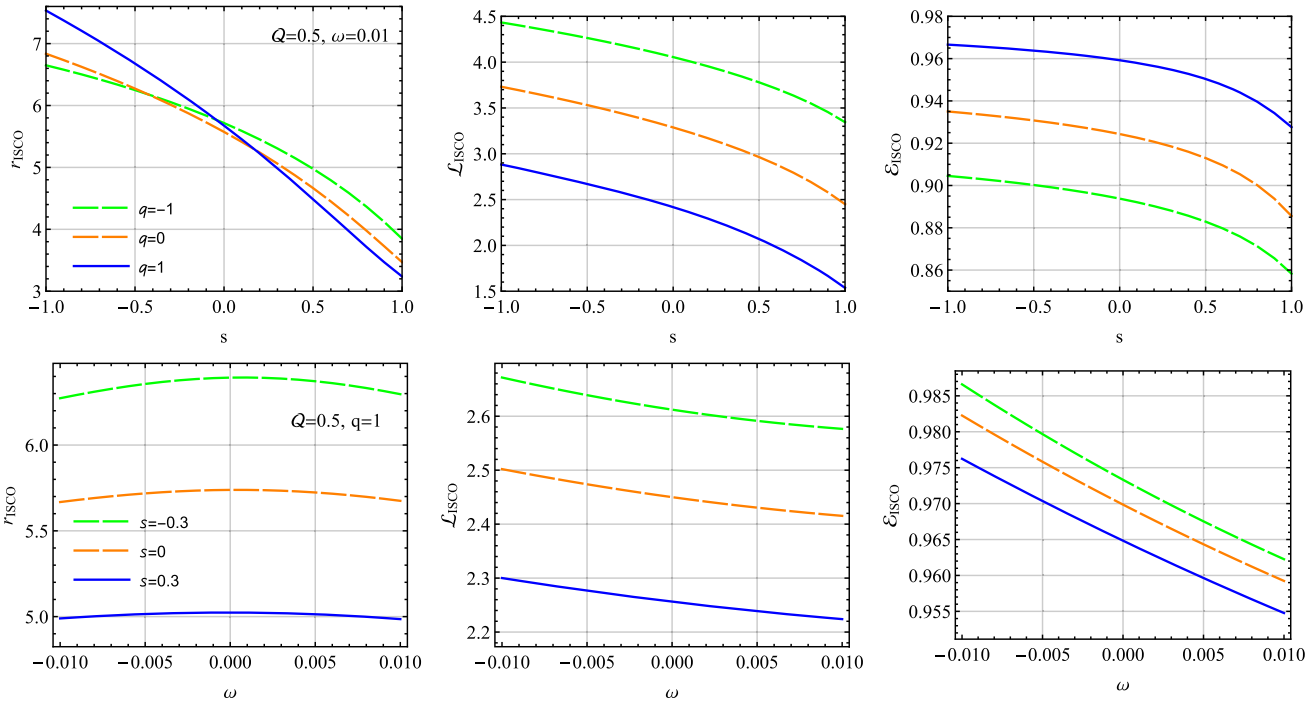

Fig. 3 ISCO parameters for a charged, spinning test particle in magnetized Reissner–Nordström spacetime. Top row: Specific energy $\mathcal{E}_{\rm ISCO}$ (left), specific angular momentum $\mathcal{L}_{\rm ISCO}$ (middle), and radius $r_{\rm ISCO}$ (right) as functions of spin s for several fixed magnetic couplings ω. Bottom row: The same three quantities as functions of ω for several fixed spins s. Unless stated otherwise, non-varied parameters (e.g., Q, q) are held fixed across panels. When ω is varied, the scan specifies whether the change is implemented via q or B_0; the physics enters through $\omega = q\,B_0$

4 Collision of charged spinning particles

The Penrose process provides a mechanism to extract rotational energy from a Kerr black hole by utilizing its ergosphere [53]. When a particle enters this region, it may split such that one fragment with negative energy falls into the black hole, reducing its angular momentum. In contrast, the other escapes with greater energy, potentially exceeding the initial input by 20–30% [54]. This effect has been extended to electromagnetic extraction through the Blandford–Znajek mechanism, where magnetic fields play a central role in powering astrophysical jets [55]. Charged or magnetized particles experience enhanced extraction efficiencies near Kerr black holes. Simulations by East and Pretorius indicate that high-energy collisions within the ergosphere amplify the energy release, although gravitational radiation limits the efficiency [56]. The process is crucial in explaining jet production in active galactic nuclei, although practical limitations, such as fine-tuning and backreaction, reduce realistic efficiencies [57,58].

A distinct route, the Bañados–Silk–West mechanism, suggests that collisions near the horizon of an extremal Kerr black hole can reach arbitrarily high center-of-mass energies when one particle has critical angular momentum [59]. This relies on strong relativistic effects near ISCOs [60]. In magnetized Kerr spacetimes, interactions between magnetic fields and charged particles further raise collision energies, sometimes by orders of magnitude [61]. Spinning particles can achieve efficiencies up to 14 times their rest energy in idealized scenarios, though astrophysical conditions reduce this [62]. Potential observational signatures include ultra-high-energy cosmic rays and gamma-ray bursts [58], although gravitational radiation and non-extremal horizons impose limits [58].

Head-on collisions and scattering near black holes also drive significant energy release, with center-of-mass energy influencing accretion, jet formation, and gravitational wave emission [63–66]. Magnetic dipole moments enhance this energy, modifying ISCO structure and extraction rates [64–68]. In accretion disks, strong magnetic fields (10^4–10^8 G) naturally generate magnetized particle populations, further amplified by reconnection processes [69,70]. Observational evidence from X-ray binaries and active galactic nuclei supports the presence of magnetized plasmas [58,71].

In this section, we study the center-of-mass energy $\mathcal{E}_{\rm cm}$ released during the collision of two charged spinning test particles in the spacetime of a RN black hole immersed in an external, asymptotically uniform magnetic field. Both parti-

cles are assumed to have equal rest mass, $m_1 = m_2 = m$, and interact with the background geometry via their mass, spin, and electric charge. The dynamics are influenced by both gravitational and electromagnetic forces, including spin-curvature coupling and Lorentz interactions.

The MPD equations with the Tulczyjew spin supplementary condition govern the spin-curvature interaction. Electromagnetic coupling is introduced through a vector potential corresponding to a uniform test magnetic field aligned along the black hole's axis. In this charged spacetime, the form of the magnetic potential is modified due to the black hole's electric charge Q, affecting the motion of charged particles even in the absence of black hole rotation.

The covariant components of the generalized momentum of the particle p_t, p_ϕ, and p_r are derived from the extended MPD formalism, which incorporates contributions from spin, electric charge, and magnetic interaction. These components, detailed in Eqs. (27) and (28), serve as the key ingredients in evaluating both orbital dynamics and collision energetics.

The center-of-mass energy of the two-particle system is computed using the general relativistic expression:

$$\mathcal{E}_{\rm cm}^2 = \frac{E_{\rm cm}^2}{2m^2} = 1 - g^{tt}u_t^{(1)}u_t^{(2)} - g^{rr}u_r^{(1)}u_r^{(2)} - g^{\phi\phi}u_\phi^{(1)}u_\phi^{(2)}, \quad (37)$$

where $u_\mu^{(i)}$ are the covariant components of the specific four-momentum of the i-th particle, and $g^{\mu\nu}$ are the inverse metric components of the RN solution.

This formulation captures the complete set of interactions contributing to the center-of-mass energy at the collision point, including spin–spin, charge–charge, and spin-magnetic effects. In particular, the ϕ components encode azimuthal desynchronization induced by the external field, even though the background is non-rotating.

4.1 Critical angular momentum

Before analyzing the detailed behavior of $\mathcal{E}_{\rm cm}$, it is essential to establish the conditions under which a charged spinning particle can physically approach the black hole. One of the key constraints is the *critical angular momentum*, denoted $\mathcal{L}_{\rm cr}$, which represents the maximum angular momentum a particle can possess while still being able to fall into the black hole from a given position. Particles with $\mathcal{L} > \mathcal{L}_{\rm cr}$ are repelled by centrifugal and electromagnetic barriers, whereas those with $\mathcal{L} \le \mathcal{L}_{\rm cr}$ can potentially reach the horizon.

This condition arises from the requirement that the squared radial velocity $\dot{r}^2$ be non-negative. The critical case corresponds to marginal capture and is determined by solving the system:

$$\dot{r}^2 = 0, \quad \frac{d\dot{r}^2}{dr} = 0,$$

which identifies a local maximum or minimum of the effective potential. This condition is particularly important when considering collisions near the horizon or at the ISCO, where small variations in spin or magnetic coupling may prevent a particle from reaching the target radius altogether.

Figure 4 illustrates how the critical angular momentum $\mathcal{L}_{\rm cr}$ depends on s, ω, and Q.

Left panel with $Q = 0.5$ and $q = 0.3$: $\mathcal{L}_{\rm cr}$ decreases monotonically as s increases; negative s requires larger $\mathcal{L}_{\rm cr}$, whereas aligned spin with $s > 0$ lowers the threshold via spin-curvature coupling. No secondary maximum is observed over the displayed range.

Right panel with $s = 0.1$ and $Q = 0.5$: in the small-ω regime appropriate to the test-field limit, $\mathcal{L}_{\rm cr}$ decreases nearly linearly with ω for like-charged cases with $qQ > 0$. A larger q steepens this decline, reflecting a stronger Lorentz coupling that weakens the effective barrier.

Overall, spin and magnetic interaction jointly reshape the capture threshold and must be accounted for when identifying parameter regions that admit infall and high-energy encounters.

4.2 Radial profiles of collision energy

Having identified the capture conditions, we now examine the radial dependence of $\mathcal{E}_{\rm cm}$ for collisions of charged, spinning test particles in a magnetized RN background. The first particle sets the baseline with fixed s_1, $\mathcal{L}_1$, and ω_1. The second particle's parameters are varied to expose how its charge, spin, and magnetic coupling shape the energy release. $\omega_i = q_i B_0$ encodes magnetic interaction; where only ω_i is quoted, the implementation via q_i or B_0 is specified in the scan setup.

Figure 5 summarizes the trends. Varying the second particle's charge in the upper left panel simultaneously tunes the Coulomb term $q_2 Q$ and the magnetic sense through $\omega_2 = q_2 B_0$. Larger $|q_2|$ strengthens both effects. When electric and magnetic senses cooperate with the baseline rotation, the azimuthal mismatch with the first particle is reduced and $\mathcal{E}_{\rm cm}$ falls near the horizon; reversing the sign of q_2 flips the Lorentz sense, increases the mismatch, and raises the energy.

Changing s_2 in the upper right panel isolates spin-curvature coupling: as s_2 becomes more aligned, the orbit is drawn toward the local circular frame, the relative rapidity decreases, and $\mathcal{E}_{\rm cm}$ drops; anti-aligned s_2 maintains a larger mismatch and yields higher energies.

Scanning ω_2 in the bottom left panel at fixed B_0 isolates the Lorentz contribution. Increasing $|\omega_2|$ biases the motion along the field and reduces the azimuthal mismatch, so the

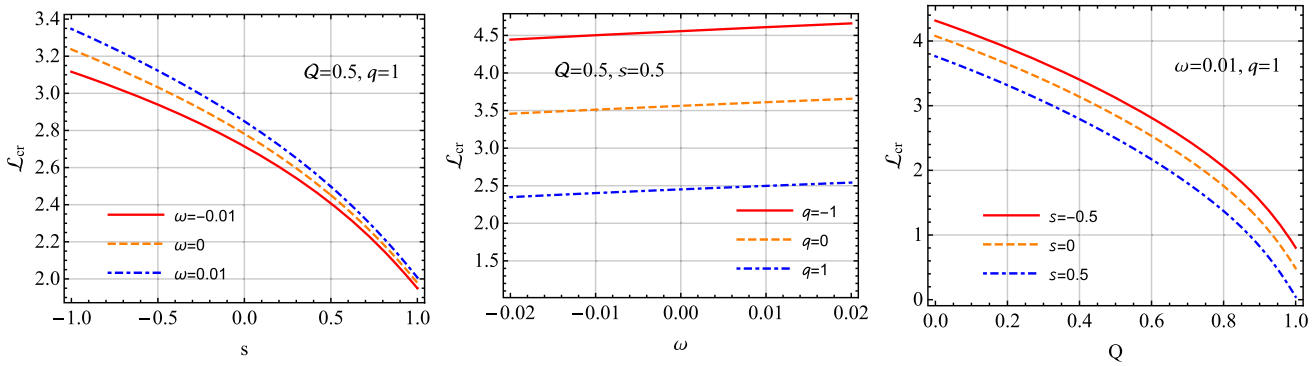

Fig. 4 Dependence of the critical angular momentum $\mathcal{L}_{\rm cr}$ on spin s, magnetic coupling ω, and black-hole charge Q for a charged, spinning test particle in magnetized Reissner–Nordström spacetime. Left: $\mathcal{L}_{\rm cr}$ versus spin s for several fixed ω (e.g. $Q = 0.5$, $q = 0.3$). Middle: $\mathcal{L}_{\rm cr}$ versus magnetic coupling ω for several fixed spins s (e.g. $Q = 0.5$ with $s \in \{-1, 0, 1\}$; particle charge held fixed). Right: $\mathcal{L}_{\rm cr}$ versus black-hole charge Q at fixed s and ω (e.g. $s = 1$, $\omega = 0.01$). Unless stated otherwise, non-varied parameters are held fixed across panels. When ω is varied, the scan indicates whether the change is implemented via q or B_0, and the physics enters through $\omega = qB_0$. Both spin and magnetic interaction shift the capture threshold and, therefore, whether a particle can reach the ISCO or the horizon

relative rapidity and $\mathcal{E}_{\rm cm}$ decline, most clearly close to the horizon. Flipping the sign of ω_2 reverses this trend.

Finally, varying Q in the bottom right panel shifts both $r_+(Q) = 1 + \sqrt{1 - Q^2}$ and the background electric field. Each curve starts outside its own horizon and $\mathcal{E}_{\rm cm}$ remains finite at r_+, consistent with near-horizon alignment of infalling worldlines. The ordering across Q reflects how the background charge modulates the same magnetic and spin mechanisms seen in the other panels.

Together, these results show how spin, magnetic coupling, and orbital orientation govern the energetics of collisions near charged, magnetized black holes. Antialigned spins, small or negative ω_2, and counter-rotating angular momenta produce the largest $\mathcal{E}_{\rm cm}$, highlighting natural routes to high-energy particle acceleration in magnetized environments.

4.3 Collisions at the ISCO

We now focus on high-energy collisions that occur precisely at the innermost stable circular orbit, where particles are naturally trapped in marginally bound orbits. Since the ISCO marks the transition between stable and unstable circular motion, it serves as a preferred site for energetic astrophysical processes, such as jet launching, hotspot formation, and radiation bursts. When two particles collide at the ISCO, the center-of-mass energy $\mathcal{E}_{\rm cm}$ can significantly increase due to the strong gravitational field and the relativistic velocities.

In this setup, we assume that the first particle has fixed spin s_1, magnetic coupling ω_1, and charge-related interaction parameter q_1, while varying the spin s_2 and charge q_2 of the second particle. For each configuration, we solve for the second particle's angular momentum so that both particles are circular at the same radius–namely, the ISCO radius set by the first particle–before collision. This ensures that both particles are physically present at the same radius, making collision kinematics meaningful.

Figure 6 follows the collision energy while we vary the second particle's spin and charge against fixed baselines, with both colliding at the same ISCO radius. In the upper left panel, $\mathcal{E}_{\rm cm}$ decreases as s_2 increases. Aligned spin tightens spin-curvature and spin-magnetic locking, narrows the azimuthal mismatch with the baseline trajectory, and reduces the invariant relative rapidity. Negative s_2 preserves the mismatch and keeps $\mathcal{E}_{\rm cm}$ higher. The contrast grows with $|\omega_1|$ because a stronger magnetic bias reinforces this locking.

Keeping ω_1 fixed but changing Q in the upper right panel repeats the s_2 sweep across different black-hole charges, again with both circular at the same ISCO radius. The monotonic decrease of $\mathcal{E}_{\rm cm}$ with increasing s_2 persists. At the same time, larger Q lowers the overall level of the curves, consistent with slightly milder relative rapidity and modified redshift and electrostatic support at the same collision radius.

Turning to charge in the bottom left panel, we scan q_2 for several ω_1 at fixed B_0 so that $\omega_2 = q_2 B_0$ varies together with q_2, maintaining circularity at the common ISCO. Over the displayed range, $\mathcal{E}_{\rm cm}$ increases with $|q_2|$ because a larger $|\omega_2|$ strengthens the Lorentz drive, pushing the two circular motions away from synchronization and raising the collision energy. A shallow minimum can appear at small $|q_2|$, reflecting a balance between the Coulomb term $q_2 Q$ and the magnetic bias.

Finally, varying Q while scanning q_2 at fixed ω_1 in the bottom right panel, again enforcing a shared ISCO, a larger Q steepens the high-$|q_2|$ rise of $\mathcal{E}_{\rm cm}$ because $q_2 Q$ amplifies the Lorentz-driven departure from synchronization. Overall, the most energetic ISCO collisions occur for anti-aligned spins and larger $|q_2|$ when the field orientation counteracts the baseline rotation.

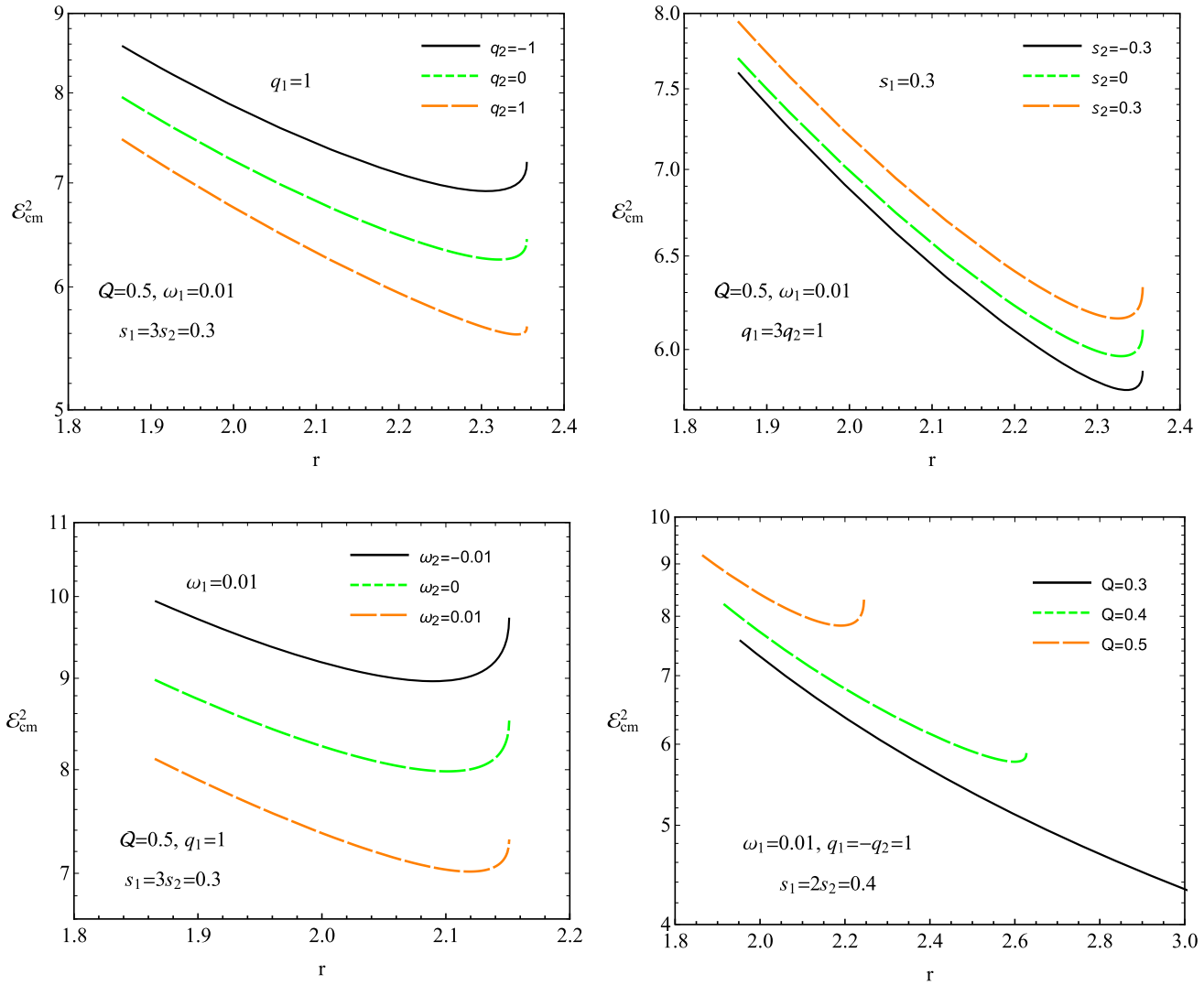

Fig. 5 Radial dependence of the center-of-mass energy $\mathcal{E}_{\rm cm}$ for collisions between spinning, charged test particles in magnetized Reissner–Nordström spacetime. Upper left: variation of q_2. Upper right: variation of s_2. Bottom left: variation of the magnetic coupling ω_2. Bottom right: variation of the black-hole charge Q. The first particle's parameters s_1, $\mathcal{L}_1$, and ω_1 are fixed throughout. When a magnetic coupling is varied, the scan indicates whether the change is realized through q_i or B_0, and the physics enters through $\omega_i = q_i B_0$. Each profile starts just outside the relevant horizon $r_+(Q)$, and $\mathcal{E}_{\rm cm}$ remains finite at r_+

5 Summary and conclusion

This work analyzed the motion and collision dynamics of charged spinning test particles in the background of an RN black hole immersed in an external magnetic field. Using the Mathisson–Papapetrou–Dixon equations with the Tulczyjew spin supplementary condition, we derived expressions for the four-momentum and four-velocity, incorporating both spin-curvature and spin-electromagnetic couplings. Throughout, the external magnetic field was treated as a test field on a fixed RN geometry, and parameter scans in $\omega \equiv q B_0$ were interpreted at fixed small B_0 by varying q.

We first studied the effective potential governing circular orbits. The results show that both spin and magnetic interaction modify the potential profile, lowering the energy and angular momentum required to sustain circular motion. These deformations shift the ISCO radius inward, reducing its energy and angular momentum, especially when the spin and magnetic coupling parameters are aligned in sign. This effect increases the binding of particles near the black hole and expands the parameter space for circular motion. For like-charged motion, increasing Q tends to shallow the well and move the minimum outward, while increasing ω generally deepens binding and shifts the minimum inward, with mild nonmonotonicity in $r_{\rm ISCO}$ at low or zero spin.

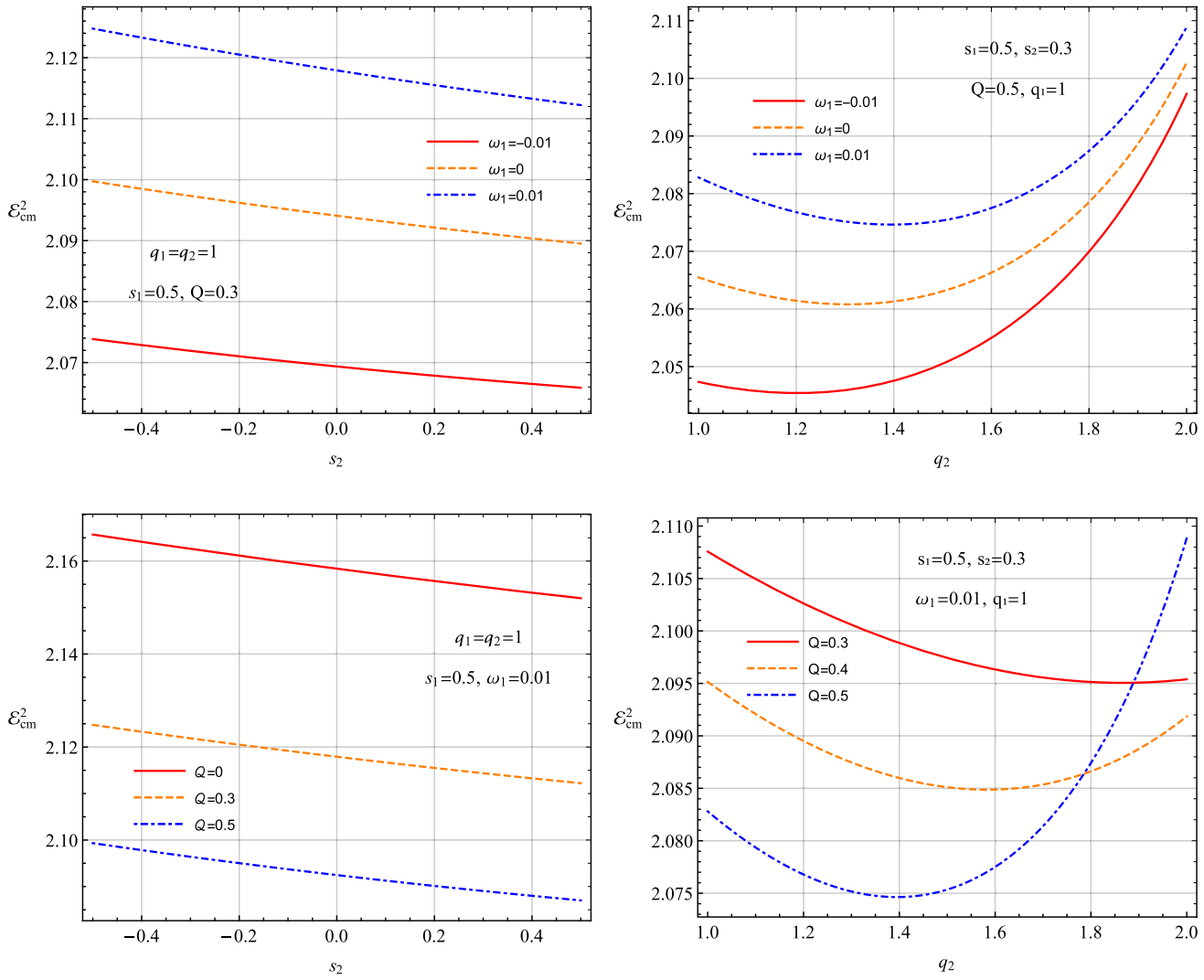

Fig. 6 Center-of-mass energy $\mathcal{E}_{\rm cm}$ for collisions of charged, spinning test particles constrained to be circular at the ISCO radius in a magnetized Reissner–Nordström background. The first particle sets the baseline ISCO and its parameters s_1, q_1, and ω_1. For each curve, the angular momentum of the second particle is then determined so that it is circular at the same radius. Magnetic interaction is encoded by $\omega_i = q_i B_0$. When a magnetic coupling is varied, the scan indicates whether the change originates from q_i or from B_0. Upper left: $\mathcal{E}_{\rm cm}$ versus s_2 for several ω_1. Upper right: $\mathcal{E}_{\rm cm}$ versus s_2 for different Q. Bottom left: $\mathcal{E}_{\rm cm}$ versus q_2 for several ω_1, with ω_2 co-varying with q_2 at fixed B_0. Bottom right: $\mathcal{E}_{\rm cm}$ versus q_2 for different Q

Next, we evaluated the critical angular momentum $\mathcal{L}_{\rm cr}$ that defines the threshold for particle infall. In contrast to a simple growth with magnetic coupling, our scans show that $\mathcal{L}_{\rm cr}$ decreases with increasing aligned spin s and, in the small-ω test-field regime and for like-charged configurations with $qQ > 0$, it also decreases nearly linearly with ω; larger q steepens this decline. These trends were interpreted in terms of spin-curvature attraction and the A_ϕ contribution reducing the mechanical angular momentum required for capture. No secondary maximum in $\mathcal{L}_{\rm cr}(s)$ was observed over the displayed range.

We then examined the radial dependence of the center-of-mass energy $\mathcal{E}_{\rm cm}$ for collisions of spinning charged particles. By varying the second particle's parameters while keeping the first fixed, we found that aligned spin with $s_2 > 0$ and larger $|\omega_2|$ tend to reduce $\mathcal{E}_{\rm cm}$ by narrowing the azimuthal mismatch, whereas anti-aligned spin and reversing the magnetic sense increase it. Maximal energy arises when the particles are counter-rotating, their spins are oppositely aligned, and the magnetic coupling of the second particle is small in magnitude or opposite in sense to the baseline. The energy peaks occur closer to the horizon and decrease with radial distance.

Finally, collisions occurring at the ISCO were analyzed. In all ISCO scans we imposed that the first and the second particle are circular at the same ISCO radius, set by the first

particle, by solving for the second particle's angular momentum. It was shown that the center-of-mass energy at the ISCO decreases with increasing s_2 for aligned spin and increases with larger $|q_2|$ when the field orientation counteracts the baseline rotation, reflecting enhanced Lorentz-driven desynchronization. These results confirm that spin-magnetic interactions can raise the energy scale of physically allowed ISCO collisions for anti-aligned spins and suitably oriented charges and fields.

Altogether, the analysis reveals how spin, magnetic interaction, and black hole charge jointly determine the conditions for orbital stability and the energetics of binary collisions in magnetized RN spacetimes. The results provide a framework for modeling particle acceleration and orbital energetics in electromagnetic environments near charged compact objects. They also clarify the parameter regime consistent with the test-field assumption, addressing the referee's concern about magnetic backreaction.

Acknowledgements J.R. thanks Grant no. F-FA-2021-510 of the Uzbekistan Agency for Innovative Development. T.O. and J.R. acknowledge the Silesian University in Opava for warm hospitality.

Data Availability Statement This paper is a pure theoretical study, and no associated code/software is involved.

Code Availability Statement Code/Software sharing does not apply to this article as no code/software was generated or analysed during the current study.

Funded by SCOAP[3].

References

1. S. Gillessen, F. Eisenhauer, S. Trippe, T. Alexander, R. Genzel, F. Martins, T. Ott, Astrophys. J. **692**, 1075 (2009). https://doi.org/10.1088/0004-637X/692/2/1075. arXiv:0810.4674 [astro-ph]
2. R. Genzel, F. Eisenhauer, S. Gillessen, Rev. Mod. Phys. **82**, 3121 (2010). https://doi.org/10.1103/RevModPhys.82.3121. arXiv:1006.0064 [astro-ph.GA]
3. M. Mathisson, Gen. Relativ. Gravit. **42**, 1011 (2010). https://doi.org/10.1007/s10714-010-0939-y
4. A. Papapetrou, Proc. R. Soc. Lond. Ser. A **209**, 248 (1951). https://doi.org/10.1098/rspa.1951.0200
5. E. Corinaldesiand, A. Papapetrou, Proc. R. Soc. Lond. Ser. A **209**, 259 (1951). https://doi.org/10.1098/rspa.1951.0201
6. W. Tulczyjew, Acta Phys. Polon. **18**, 393 (1959)
7. B. Tulczyjewand, W.M. Tulczyjew, *Recent Developments in General Relativity: A Collection of Papers Dedicated to Leopold Infeld* (PWN-Polish Scientific Publishers, Pergamon Press, Warsaw, 1962), pp.465–472
8. C. Møller, On the definition of the centre of gravity of an arbitrary closed system in the theory of relativity. Technical Report 5, Dublin Institute for Advanced Studies, Dublin (1949)
9. W. Beiglböck, Commun. Math. Phys. **5**, 106 (1967). https://doi.org/10.1007/BF01646841
10. W.G. Dixon, Il Nuovo Cimento **34**, 317 (1964). https://doi.org/10.1007/BF02734579
11. W.G. Dixon, Proc. R. Soc. Lond. Ser. A **314**, 499 (1970). https://doi.org/10.1098/rspa.1970.0020
12. W.G. Dixon, Proc. R. Soc. Lond. Ser. A **319**, 509 (1970). https://doi.org/10.1098/rspa.1970.0191
13. J. Ehlersand, E. Rudolph, Gen. Relativ. Gravit. **8**, 197 (1977). https://doi.org/10.1007/BF00763547
14. W.G. Ramírezand, A.A. Deriglazov, Phys. Rev. D **96**, 124013 (2017). https://doi.org/10.1103/PhysRevD.96.124013. arXiv:1709.06894 [gr-qc]
15. A.A. Deriglazovand, W.G. Ramírez, Phys. Lett. B **779**, 210 (2018). https://doi.org/10.1016/j.physletb.2018.01.063. arXiv:1802.08079 [gr-qc]
16. B. Toshmatovand, D. Malafarina, Phys. Rev. D **100**, 104052 (2019). https://doi.org/10.1103/PhysRevD.100.104052. arXiv:1910.11565 [gr-qc]
17. H. Nazar, A. Majeed, G. Abbas, A. Ashraf, A.A. Ibraheem, E. Davletov, Chin. J. Phys. **96**, 1083 (2025). https://doi.org/10.1016/j.cjph.2025.06.008
18. G.V. Kraniotisand, S.B. Whitehouse, Class. Quantum Gravity **20**, 4817 (2003). https://doi.org/10.1088/0264-9381/20/22/007. arXiv:astro-ph/0305181
19. G.V. Kraniotis, Class. Quantum Gravity **21**, 4743 (2004). https://doi.org/10.1088/0264-9381/21/19/016. arXiv:gr-qc/0405095
20. N. Cruz, M. Olivares, J.R. Villanueva, Class. Quantum Gravity **22**, 1167 (2005). https://doi.org/10.1088/0264-9381/22/6/016. arXiv:gr-qc/0408016
21. E. Hackmannand, C. Lämmerzahl, Phys. Rev. Lett. **100**, 171101 (2008). https://doi.org/10.1103/PhysRevLett.100.171101. arXiv:1505.07955 [gr-qc]
22. E. Hackmannand, C. Lämmerzahl, Phys. Rev. D **78**, 024035 (2008). https://doi.org/10.1103/PhysRevD.78.024035. arXiv:1505.07973 [gr-qc]
23. E. Hackmann, V. Kagramanova, J. Kunz, C. Lämmerzahl, EPL (Europhys. Lett.) **88**, 30008 (2009). https://doi.org/10.1209/0295-5075/88/30008. arXiv:0911.1634 [gr-qc]
24. E. Hackmann, B. Hartmann, C. Lämmerzahl, P. Sirimachan, Phys. Rev. D **81**, 064016 (2010). https://doi.org/10.1103/PhysRevD.81.064016. arXiv:0912.2327 [gr-qc]
25. M. Olivares, J. Saavedra, C. Leiva, J.R. Villanueva, Mod. Phys. Lett. A **26**, 2923 (2011). https://doi.org/10.1142/S0217732311037261. arXiv:1101.0748 [gr-qc]
26. B. Hoseini, R. Saffari, S. Soroushfar, Class. Quantum Gravity **34**, 055004 (2017). https://doi.org/10.1088/1361-6382/aa5a63. arXiv:1606.06558 [gr-qc]
27. M. Fathi, M. Olivares, J.R. Villanueva, N. Cruz, Eur. Phys. J. Plus **139**, 752 (2024). https://doi.org/10.1140/epjp/s13360-024-05541-0. arXiv:2311.14017 [gr-qc]
28. M. Fathi, M. Olivares, J.R. Villanueva, Eur. Phys. J. C **81**, 987 (2021). https://doi.org/10.1140/epjc/s10052-021-09787-1. arXiv:2104.07721 [gr-qc]
29. M. Fathi, M. Olivares, J.R. Villanueva, Eur. Phys. J. C **82**, 629 (2022). https://doi.org/10.1140/epjc/s10052-022-10600-w. arXiv:2205.13261 [gr-qc]

30. U. Uktamov, M. Fathi, J. Rayimbaev, A. Abdujabbarov, Phys. Rev. D **110**, 084084 (2024). https://doi.org/10.1103/PhysRevD.110.084084. arXiv:2406.03371 [gr-qc]
31. C.G. J. Jacobi, *Gesammelte Werke*, vol. 1, edited by C.W. Borchardt (G. Reimer, Berlin, 1881)
32. N.H. Abel, in *Oeuvres complètes de Niels Henrik Abel*, edited by L. Sylowand, S. Lie (Grøndahl & Søn, Christiania, 1881)
33. B. Riemann, j. für die reine und angewandte Mathematik **54**, 115 (1857)
34. B. Riemann, J. für die reine und angewandte Mathematik **65**, 161 (1866)
35. C. Weierstrass, Journal für die reine und angewandte Mathematik **47**, 289 (1854)
36. H.F. Baker, *Abel's Theorem and the Allied Theory, Including the Theory of the Theta Functions* (Cambridge University Press, Cambridge, 1897)
37. R.M. Wald, *General Relativity* (University of Chicago Press, Chicago, 1984)
38. M. Boboqambarova, B. Turimov, A. Abdujabbarov, Mod. Phys. Lett. A **38**, 2350071 (2023). https://doi.org/10.1142/S0217732323500712. arXiv:2110.05764 [gr-qc]
39. S. Murodov, A.H. Bokhari, J. Rayimbaev, B. Ahmedov, Eur. Phys. J. C **85**, 551 (2025). https://doi.org/10.1140/epjc/s10052-025-14298-4
40. N. Kurbonov, A.H. Bokhari, J. Rayimbaev, B. Ahmedov, Eur. Phys. J. C **85**, 494 (2025). https://doi.org/10.1140/epjc/s10052-025-14231-9
41. S. Mitra, J. Vrba, J. Rayimbaev, Z. Stuchlik, B. Ahmedov, Phys. Dark Universe **46**, 101561 (2024). https://doi.org/10.1016/j.dark.2024.101561
42. J. Rayimbaev, S. Murodov, A. Shermatov, A. Yusupov, Eur. Phys. J. C **84**, 1114 (2024). https://doi.org/10.1140/epjc/s10052-024-13463-5
43. Z. Stuchlík, M. Kološ, J. Kovář, P. Slaný, A. Tursunov, Universe **6**, 26 (2020). https://doi.org/10.3390/universe6020026
44. Z. Stuchlík, M. Kološ, A. Tursunov, Universe **7**, 416 (2021). https://doi.org/10.3390/universe7110416
45. R. Hojmanand, S. Hojman, Phys. Rev. D **15**, 2724 (1977). https://doi.org/10.1103/PhysRevD.15.2724
46. M. Saijo, K.-I. Maeda, M. Shibata, Y. Mino, Phys. Rev. D **58**, 064005 (1998). https://doi.org/10.1103/PhysRevD.58.064005
47. B. Turimov, Z. Stuchlík, J. Rayimbayev, A. Abdujabbarov, Phys. Rev. D **103**, 124039 (2021). https://doi.org/10.1103/PhysRevD.103.124039
48. J.M. Ladino, C.A. Benavides-Gallego, E. Larrañaga, J. Rayimbaev, F. Abdulxamidov, Eur. Phys. J. C **83**, 989 (2023). https://doi.org/10.1140/epjc/s10052-023-12187-2. arXiv:2305.15350 [gr-qc]
49. C. Conde, C. Galvis, E. Larrañaga, Phys. Rev. D **99**, 104059 (2019). https://doi.org/10.1103/PhysRevD.99.104059. arXiv:1905.01323 [gr-qc]
50. T. Oteev, F. Abdulkhamidov, J. Rayimbaev, Z. Stuchlík, B. Ahmedov, Phys. Dark Universe **46**, 101588 (2024). https://doi.org/10.1016/j.dark.2024.101588
51. T. Oteev, Z. Stuchlík, J. Rayimbaev, I. Ibragimov, M. Sharibaev, A. Abdujabbarov, Eur. Phys. J. C **85**, 953 (2025). https://doi.org/10.1140/epjc/s10052-025-14660-6
52. F. Abdulxamidov, J. Rayimbaev, A. Abdujabbarov, Z. Stuchlík, Phys. Rev. D **108**, 044030 (2023). https://doi.org/10.1103/PhysRevD.108.044030. arXiv:2308.05392 [gr-qc]
53. R. Penrose, Gen. Relativ. Gravit. **7**, 1141 (2002). https://doi.org/10.1023/A:1016578408204
54. T. Piranand, J. Shaham, Phys. Rev. D **16**, 1615 (1977). https://doi.org/10.1103/PhysRevD.16.1615
55. R.D. Blandfordand, R.L. Znajek, **179**, 433 (1977). https://doi.org/10.1093/mnras/179.3.433
56. W.E. Eastand, F. Pretorius, Phys. Rev. Lett. **110**, 101101 (2013). https://doi.org/10.1103/PhysRevLett.110.101101. arXiv:1210.0443 [gr-qc]
57. K.-I. Nakao, H. Okawa, K.-I. Maeda, Prog. Theor. Exp. Phys. **2018**, 013E01 (2018). https://doi.org/10.1093/ptep/ptx170. arXiv:1708.04003 [gr-qc]
58. J.D. Schnittman, Gen. Relativ. Gravit. **50**, 77 (2018). https://doi.org/10.1007/s10714-018-2373-5. arXiv:1910.02800 [astro-ph.HE]
59. M. Bañados, J. Silk, S.M. West, Phys. Rev. Lett. **103**, 111102 (2009). https://doi.org/10.1103/PhysRevLett.103.111102. arXiv:0909.0169 [hep-ph]
60. B. Turimovand, S. Hayitov, arXiv e-prints (2023). https://doi.org/10.48550/arXiv.2307.01919. arXiv:2307.01919
61. B. Narzilloev, A. Abdujabbarov, C. Bambi, B. Ahmedov, Phys. Rev. D **99**, 104009 (2019). https://doi.org/10.1103/PhysRevD.99.104009. arXiv:1902.03414 [gr-qc]
62. E. Leiderschneiderand, T. Piran, Phys. Rev. D **93**, 043015 (2016). https://doi.org/10.1103/PhysRevD.93.043015
63. M. Bejger, T. Piran, M. Abramowicz, F. Håkanson, Phys. Rev. Lett. **109**, 121101 (2012). https://doi.org/10.1103/PhysRevLett.109.121101. arXiv:1205.4350 [astro-ph.HE]
64. S. Rakhmanov, K. Matchonov, H. Yusupov, K. Nasriddinov, D. Matrasulov, Eur. Phys. J. B **98**, 35 (2025). https://doi.org/10.1140/epjb/s10051-025-00885-7. arXiv:2504.03599 [cond-mat.mes-hall]
65. B. Rahmatov, M. Zahid, S.U. Khan, J. Rayimbaev, I. Ibragimov, Z. Yuldoshev, A. Dauletov, S. Muminov, Chin. Phys. C **49**, 075105 (2025). https://doi.org/10.1088/1674-1137/adc188
66. S. Jumaniyozov, S. Murodov, J. Rayimbaev, I. Ibragimov, B. Madaminov, S. Urinbaev, A. Abdujabbarov, Eur. Phys. J. C **85**, 797 (2025). https://doi.org/10.1140/epjc/s10052-025-14522-1
67. J. Rayimbaev, B. Narzilloev, A. Abdujabbarov, B. Ahmedov, Galaxies **9**, 71 (2021). https://doi.org/10.3390/galaxies9040071
68. S.U. Khan, O. Abdurkhmonov, J. Rayimbaev, S. Ahmedov, Y. Turaev, S. Muminov, Eur. Phys. J. C **84**, 650 (2024). https://doi.org/10.1140/epjc/s10052-024-12997-y
69. M.E. Akramov, J.R. Yusupov, M. Ehrhardt, H. Susanto, D.U. Matrasulov, **100**, 045209 (2025). https://doi.org/10.1088/1402-4896/adb914. arXiv:2408.03709 [math-ph]
70. S. Shaymatov, M. Alloqulov, B. Ahmedov, A. Wang, Phys. Rev. D **110**, 044005 (2024). https://doi.org/10.1103/PhysRevD.110.044005. arXiv:2307.03012 [gr-qc]
71. B. Turimov, S. Usanov, Y. Khamroev, Phys. Dark Universe **48**, 101876 (2025). https://doi.org/10.1016/j.dark.2025.101876. arXiv:2502.11185 [gr-qc]